Trade Wind Boundary Layer Turbulence and Shallow Convection: New Insights Combining SAR Images, Satellite Brightness Temperature and Airborne In Situ Measurements

P.-E. Brilouet[1], D. Bouniol[1], F. Couvreux[1], A. Ayet[2,3], C. Granero-Belinchon[4], M.Lothon[5]and A. Mouche[6]

[1]CNRM, Université de Toulouse, Météo-France, CNRS, Toulouse, France
[2]CNRS, Université Grenoble Alpes, Inria, Grenoble INP, GIPSA-Lab, Grenoble, France
[3]CECI, Université de Toulouse, CNRS, CERFACS, Toulouse, France
[4]Mathematical and Electrical Engineering Department, IMT Atlantique, Lab-STICC, UMR CNRS 6285, 29238 Brest, France
[5]Laboratoire d'Aérologie, University of Toulouse, CNRS, UPS, Toulouse, France
[6]Ifremer, Univ. Brest, CNRS, IRD, Laboratoire d'Océanographie Physique et Spatiale (LOPS), IUEM, Brest 29280, France

Key Points:

- Atmospheric coherent structures, rolls and cold pools are systematically detected and analyzed in a high-resolution SAR wide swath image
- Properties of rolls from SAR measurements are comparable with the circulation organization deduced from airborne data
- A diversity of cold pool geometrical and dynamical features is related to cloud life cycle provided by satellite brightness temperature

Corresponding author: P.-E. Brilouet, pierre-etienne.brilouet@aero.obs-mip.fr

Abstract

The imprint of marine atmospheric boundary layer (MABL) dynamical structures on sea surface roughness, as seen from Sentinel-1 Synthetic Aperture Radar (SAR) acquisitions, is investigated. We focus on February 13th, 2020, a case study of the EUREC4A (Elucidating the role of clouds-circulation coupling in climate) field campaign. For suppressed conditions, convective rolls imprint on sea surface roughness is confirmed through the intercomparison with MABL turbulent organization deduced from airborne measurements. A discretization of the SAR wide swath into 25 x 25 km^2 tiles then allows us to capture the spatial variability of the turbulence organization varying from rolls to cells. Secondly, we objectively detect cold pools within the SAR image and combine them with geostationary brightness temperature. The geometrical or physically-based metrics of cold pools are correlated to cloud properties. This provides a promising methodology to analyze the dynamics of convective systems as seen from below and above.

Plain Language Summary

We propose an innovative approach to investigate the marine atmospheric boundary layer dynamics by combining spaceborne Synthetic Aperture Radar (SAR) images, brightness temperature from the Geostationary Operational Environmental Satellite (GOES) and in situ turbulence airborne measurements. Focusing on February 13th, 2020, two types of atmospheric processes are investigated: trade wind boundary layer organizations and cold pools. The signature of coherent structures on sea surface roughness, especially convective rolls, is validated with respect to the turbulence airborne measurements. The cold pools are detected within the SAR image using an identification technique based on the filtering of backscatter signal increments. Cold pool characteristics such as their size or the gust front intensity can then be directly derived from the SAR image. The GOES images provide cloud field properties every 10 min. Exploring backward cloud evolution with respect to the SAR image timing appears meaningful to catch the life cycle of cold pools and convective clouds from which they originate. The application of this approach could pave the way to access the dynamics of convective systems as seen from below and above, allowing to go one step further in the quantitative use of SAR images to investigate boundary layer processes.

1 Introduction

Marine atmospheric boundary layer (MABL) dynamics plays a crucial role in the mesoscale organization of convection. Among the different kinds of coherent organizations occurring inside the MABL, three-dimensional cells and quasi-two-dimensional convective rolls are frequent (Young et al., 2002), and can be interlocked depending on the stability conditions (Grossman, 1982). Another important MABL coherent structures are the cold pools, which are key components for the life cycle of convection and cloud organization. Cold pools are generated by the downward motion of air mass cooled by rain evaporation. At the surface, it spreads out horizontally to form a gust front with an enhanced wind intensity. Numerous previous studies have addressed the oceanic cold pools associated with deep convection but fewer have focused on shallow convection. In the winter trades, suppressed conditions can be predominant, leading to shallow convective activity in a subsiding large-scale environment. Particular mesoscale cloud organization can occur (Stevens et al., 2020), surrounded by clear skies or small fair-weather cumuli. It is then fundamental to improve the monitoring of cold pools and their interplay with convection systems.

To improve our understanding of MABL coherent structures, accurate measurements are needed. Airborne measurements have been widely used to characterize the MABL turbulent structure (e.g., LeMone & Pennell, 1976; Grossman, 1982). The cold pool properties have been mainly documented through shipboard (e.g., Zuidema et al., 2012; de

Szoeke et al., 2017) and shore-based measurements (e.g., Vogel et al., 2021). Most observational studies are based on in-situ data, with a spatially-limited sampling. For the shallow convection, high-resolution spaceborne observations of sea-surface roughness seem relevant. In particular, Synthetic Aperture Radar (SAR) backscatter is such a high resolution ($\sim$ 10 m – 100 m) measurements available during day and night, regardless of weather conditions and cloud cover. Atmospheric coherent structures induce a contrast of SAR backscatter. Atlas (1994) was a pioneer in highlighting the potential signature of a storm microburst on the sea surface. Previous works focused on convective rolls (Alpers & Brümmer, 1994; Young et al., 2000; Vandemark et al., 2001; Wang et al., 2020) and on deep convective cold pools from SAR winds (La et al., 2020) or from scatterometer winds (Mapes et al., 2009; Kilpatrick & Xie, 2015; Garg et al., 2020).

Systematic and quantitative extraction of MABL properties in SAR measurements is still a challenge, since they are multi-scale and superimpose with oceanic signatures (Kudryavtsev et al., 2005). The aim of this paper is to present an innovative approach based on a combined use of SAR, geostationary satellite data and airborne measurements to study the interplay between the MABL and convective organization. By doing so we (i) show how SAR compares to aircraft in situ measurements under suppressed conditions and (ii) analyse the morphological and dynamical properties of cold pools, related to moist convection.

The paper is organized as follows: the data and methods are presented in Section 2. Section 3 is devoted to the boundary layer circulations under suppressed conditions and Section 4 addresses the cold pool detection and characterization. The last section concludes the paper with a discussion of the main results.

2 Data and Methods

2.1 Data

We used a C-band SAR image from the Sentinel-1 satellite in interferometric wide swath (IW) mode. The image is 400-km wide with an effective resolution of 100 m. The backscatter signal (σ_0) is sensitive to the slope distribution of cm-scale waves, with short adjustment timescales to changes in surface wind (Kudryavtsev et al., 2005). The wind field could have been estimated from σ_0, using a Geophysical Model Function (GMF). Nevertheless, those wind retrieval algorithm have been designed for low-resolution ($\sim$ 25$-$50 km) scatterometers and are not yet adapted to high resolution. As the high resolution is required for the present study, we thus focus on backscatter contrasts which can be related to surface signatures of MABL processes (Ayet et al., 2021).

The infrared brightness temperature (T_B) provided by the Advanced Baseline Imager (ABI, Schmit et al., 2005) onboard GOES-16 (Geostationary Operational Environmental Satellite) is used to document the cloud layer. The spatial resolution is 2×2 km^2 and temporal resolution 10 min. In the Atlantic trades, low-level clouds are predominant and can be detected despite their small temperature differences with the sea surface. It should be kept in mind that, given its spatial resolution, areas that appear to be clear skies may contain small isolated fair-weather cumuli.

In addition, we used surface wind speed and direction estimated from WindSat, a polarimetric microwave radiometer operated on the Coriolis satellite, with a spatial resolution of 25×25 km^2 (Wentz et al., 2013).

Finally, we used in situ observations from the SAFIRE ATR 42 aircraft, collected during the Elucidating the role of clouds-circulation coupling in climate (EUREC4A) campaign (Bony et al., 2022). Two MABL levels were sampled, one near its top (around 600 m) and the other near the middle (around 300 m). The aircraft flew L-shape patterns composed of two straight legs perpendicular to each other, along and across the mean

wind direction (orange and brown lines in Fig. 1a, respectively). We will focus on the vertical velocity fluctuations (w') deduced from a five-hole radome nose with a spatial resolution of around 4 m (Brilouet et al., 2021).

Here, we focused on one case study, the February 13th 2020, with the best spatial and temporal overlapping between ATR 42 and Sentinel-1 acquisition: an ATR 42 flight between 0735 UTC and 1152 UTC and a Sentinel-1 crossing around 0935 UTC, about 100 km away from the aircraft track (see Fig. 1a). Based on in situ EUREC4A data, a T_B threshold of 292 K has been chosen : colder pixels are considered cloudy. Superimposing T_B and σ_0 allows us to study the clouds and their associated cold pools as well as convective rolls under small cumulus or clear sky.

2.2 Methods

2.2.1 Characteristics from two-dimensional autocorrelation

In order to capture the spatial variability, the wide swath SAR image has been split into 25×25 km^2 tiles (Fig. 2a). This is a good compromise with sub-domains that are large enough to properly sample coherent structures and small enough to be homogeneous. Using the GOES image, tiles with cloudy pixels were removed (blue tiles in Fig. 2a), allowing us to analyze the boundary layer turbulence under suppressed conditions.

Two-dimensional autocorrelation is calculated over each 25×25 km^2 tiled area. Following the methodology detailed in Granero-Belinchon et al. (2022), we first estimate the longitudinal axis of the coherent structures (noted hereafter as Ψ, Fig. 2b,c solid red line). Then, following Lohou et al. (2000), the integral lengthscale L_E is estimated for each angle θ and an elliptical fit is applied to the resulting polar curve (red ellipse in Figs. 2b,c). The type of organization is then diagnosed from the flatness parameter f of the ellipse. A threshold is empirically chosen to distinguish anisotropic structures ($f >= 0.7$, green tiles in Fig. 2a and Fig. 2c) from the transition between rolls and cells ($f < 0.7$, orange tiles in Fig. 2a and Fig. 2b). The orientation of the major axis provides a second estimate of the roll direction (noted hereafter as α, dashed purple line in Figs. 2b,c). Moreover, for roll tiles, the organized structure lengthscale L_{OS} is defined as the autocorrelation secondary local maximum along the direction perpendicular to the structures (purple line in Fig.2c): it corresponds to the mean transverse wavelength of the rolls.

2.2.2 Identification and characterization of cold pools

An objective identification method of cold pools which imprints on SAR images has been developed and validated over the case study. An example of an isolated cold pool signature is given in Fig. 3a corresponding to the south area of the SAR swath (see Fig. 1a). As the trade flow is oriented in the south westward direction, the surface wind divergence associated with the cold pool induces an enhancement of the ambient wind on the western side which leads to a higher backscatter signal (i.e. bright section). In the eastern side, the backscattered signal is attenuated (i.e. dark section) as the downdraft counteracts the ambient wind (Atlas et al., 1995). The method makes the physical assumption that the pattern of a cold pool consists of strong positive gradients at its forward and backward edges (blue zones in Fig. 3c) and a rather smooth central area with a negative gradient (green zone in Fig. 3c). Those corresponds respectively to the gust front and the horizontal wind divergence associated to the downdraft. The edges are first detected by computing increments on the gaussian-filtered backscatter signal and selecting pixels with increments larger than twice the increment standard deviation. Individual cold pools objects (orange contours in Fig. 3b) are then defined by grouping edges together if a zone of negative increment exists between them (e.g., Fig. 3c, the blue edges are part of the same cold pool because of the green zone with negative increment).

Detected cold pools were contextualized with an object identification of cloud structures within GOES T_B. The method is described in Brient et al. (2019) and Villefranque et al. (2020): it uses the watershed algorithm in space and time with two thresholds on the cloud object ($T_B \leq 292$ K) and on the cold cores ($T_B \leq 285$ K). This method thus connects the instantaneous snapshot of cold pools with the temporal evolution of the cloud organization and individual cloud life cycle.

3 Clear-Sky Turbulence

The ability of SAR to retrieve fair-weather MABL coherent structures is assessed using airborne observations. Two transects were made in the SAR image to mimic the aircraft legs (Fig. 1a). The directions of the two SAR transects (blue and green lines) were chosen to have a similar orientation with respect to the local mean wind as the ATR42 (brown and orange line). They are relative to the surface wind from WindSat for the SAR image and to the averaged measured wind along the legs for the ATR42. The time series of w' and σ_0 fluctuations highlight similar signal dynamics. In both cases, ATR42 and SAR observations, the signals differ substantially between the two sampling directions: the periodicity of the sampled eddies is significantly smaller for the approximately crosswind legs (Figs. 1d and 1e) than approximately along-wind ones (Figs. 1b and 1c). This is confirmed with the autocorrelation of the signals (Figs. 1f and 1g). This emphasizes the nonaxisymmetric behavior of both MABL turbulence and sea surface roughness.

To document the uncertainties associated with the unidirectional nature of the in situ airborne sampling and to access the random scatter of individual samples, a set of 40 1D-SAR transects is extracted, perpendicular to the roll direction (contained within the pink parallelepipede in Fig. 1a). The L_{OS} computed on this set shows a substantial variability between 1.10 km and 4.71 km with an average value of 2.65 km (see the boxplot in Fig. 1f). The estimates made on the ATR legs at 300 m and 600 m are 1.60 km and 2.00 km, respectively, are well within this range of values covered by the 1D-SAR estimates. This result is in line with the study of Vandemark et al. (2001) and consolidates the hypothesis of a sea surface roughness imprint from MABL coherent structures. Based on the 2D autocorrelation over the pink area, an L_{OS} of 2.90km is estimated which is consistent with the 1D SAR range of values and with in situ estimates. In the SAR subdomain considered here, a dropsonde launched close to the SAR passage timing reveals a well-mixed MABL with a depth of $z_i = 570$ m. It leads to an aspect ratio of 5.1. For ATR42 measurements, the MABL depth estimates are variable, ranging from $z_i = 500$ m to $z_i = 800$ m. This variability can be driven by dry air intrusions from the troposphere or by secondary circulation dynamics generated by the mesoscale cloud system. Therefore, the aspect ratio estimates in the ATR42 flight area are ranging from 2 to 4. The aspect ratio is commonly between 2 to 6, with some observed extreme values higher than 10 (LeMone, 1973; Brown, 1980; Etling & Brown, 1993).

The 2D autocorrelation analysis, extended to 58 subdomains in the entire SAR image (Fig. 2a), allows us to explore the spatial variability of MABL structures. Based on the flatness criterion, convective rolls (green tiles) are the dominant type of clear sky MABL organization, given the prevailing large-scale conditions (Etling & Brown, 1993). Also, the transition zones (orange tiles) are mainly located downwind of cloud boundaries. They can be interpreted as buffer zones between the sub-cloud organization driven by the cold pools and the clear-sky rolls, only slightly disturbed by the cloud activity.

When the structures are clearly identified as convective rolls, the difference between the two independent estimates of roll orientation, Ψ and α, becomes low (Fig. 2d). The roll direction estimate is hence robust, unlike cell/roll transition cases for which defining a direction is hardly relevant. Over the study area, the surface wind direction from WindSat, exhibits only slight variations, between 50° and 75°, characteristic of the es-

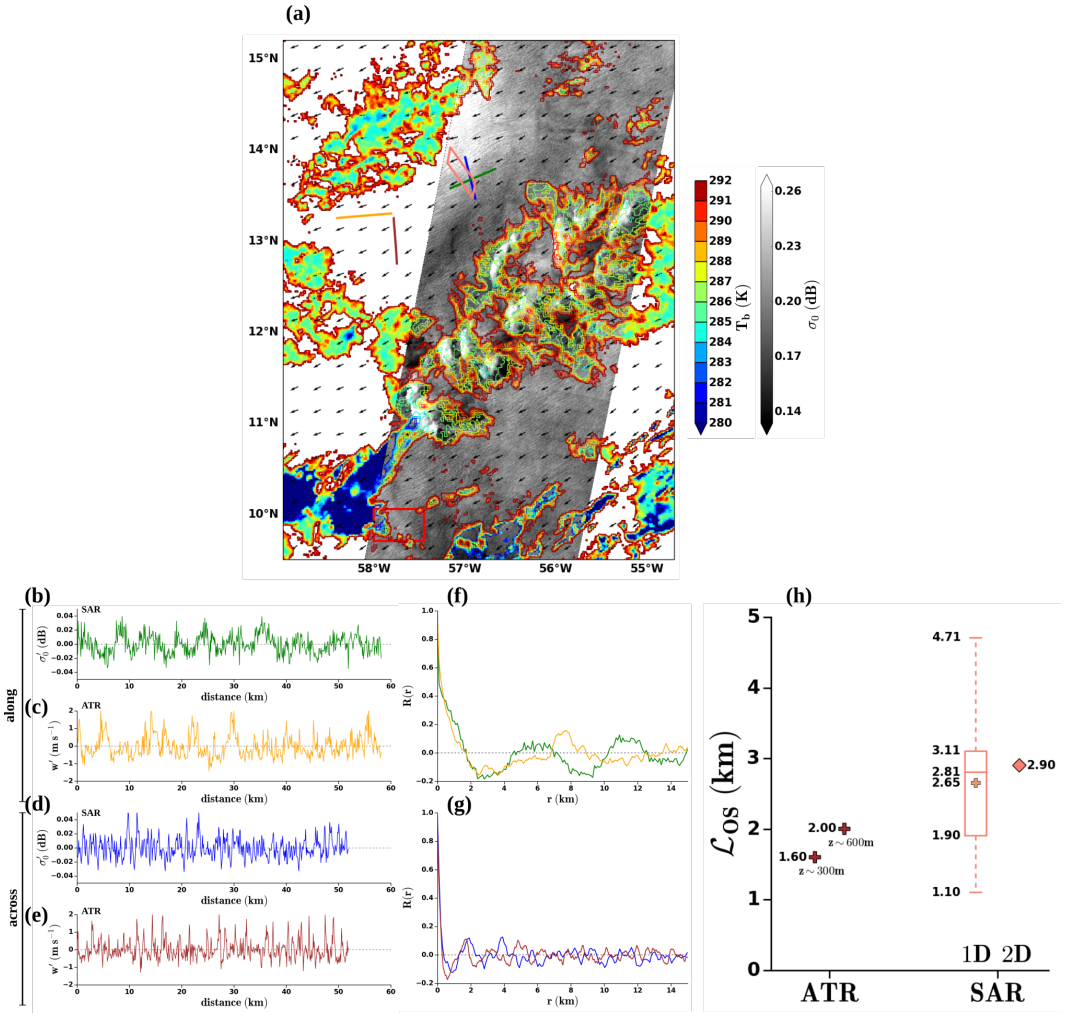

Figure 1. (a) SAR σ_0, superimposed with the GOES T_b and WindSat surface wind vector (black arrows) for February 13, 2020. The orange and brown lines denote the ATR42 legs and the green and blue lines refer to SAR transects. The pink contour represents the area over which SAR 1D and 2D autocorrelations have been computed. The red square corresponds to the region with the considered cold pool in Fig. 3. Time series of (b) and (c) along-wind σ_0' fluctuations and aircraft w'f at z $\sim$ 300 m, (d) and (e) cross-wind σ_0' and w'. (f) and (g) Autocorrelation of along-wind and cross-wind signals, respectively. The different colors correspond to the ATR and SAR transects sketched on the map (a). (h) Organized structure lengthscale (L_{OS}) estimates from the ATR 42 (brown cross markers) and from SAR with 1D and 2D autocorrelations in the pink area.

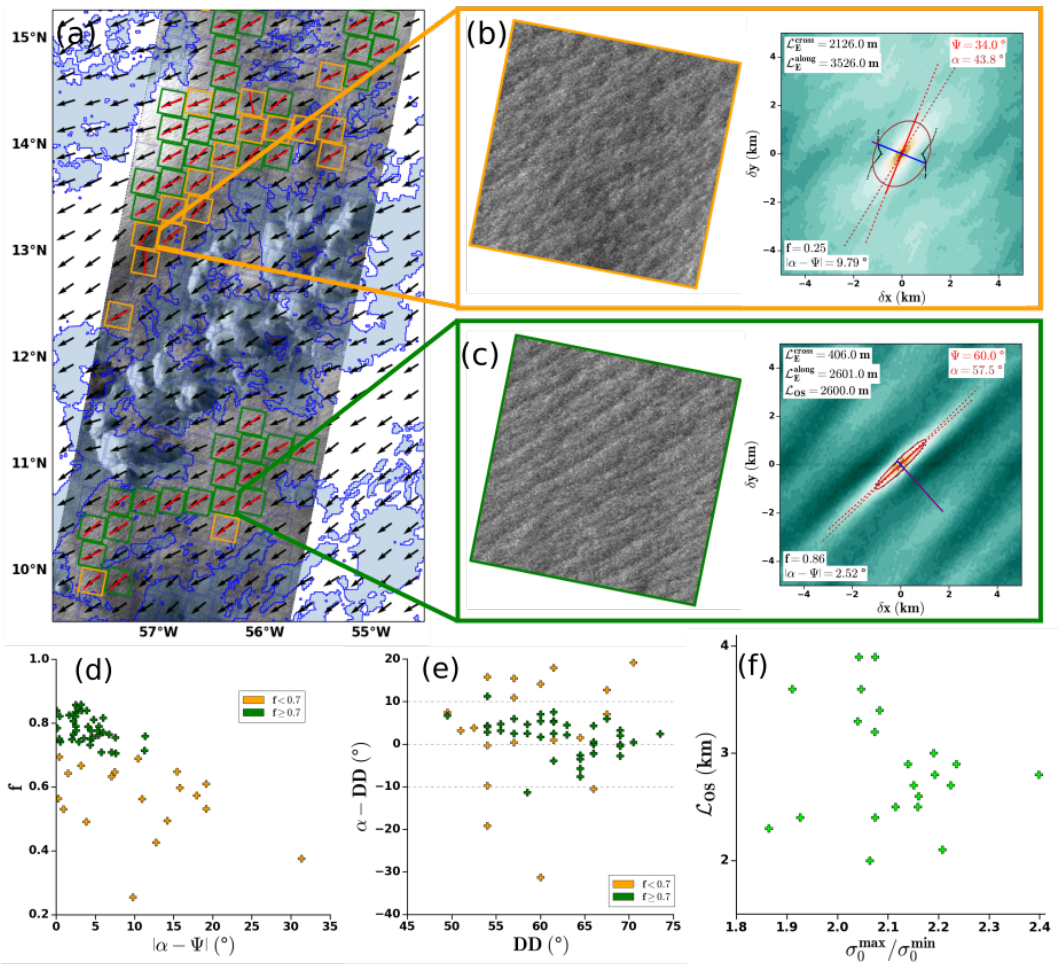

Figure 2. (a) SAR image with an organization criterion: cell / roll transition ($f < 0,7$) in orange and rolls ($f >= 0.7$) in green. The black arrows are the WindSat surface wind and the red lines are the roll directions. Examples of $\sigma 0$ and associated 2D autocorrelation for (b) a cell / roll transition regime and (c) a well-established rolls regime. (d) Flatness versus the difference between the two estimates of structure directions, (e) difference between the structure direction and the wind direction and (f) L_{OS} according to the ratio $\max(\sigma_0)$ / $\min(\sigma_0)$.

tablished trade-wind flow. The roll axis is mostly oriented along the WindSat surface wind, with a slight positive bias and a variability that can reach $\pm 10°$ (Fig. 2e), in line with previous studies (Alpers & Brümmer, 1994; Atkinson & Wu Zhang, 1996; Wang et al., 2019). Over the 39 tiled areas detected as anisotropic structures, 22 have a well-marked periodicity scale ($\mathcal{L}_{OS}$) and are unambiguously rolls. The remaining 17 tiles contain stretched structures along the mean wind direction which can be either rows of cells or a combination of rolls with different sizes. In order to relate the roll size evolution to the dynamic conditions, L_{OS} is shown in Fig. 2f as a function of the ratio between the maximum and the minimum of σ_0 over each tile. We assume that a higher modulation of the roughness is associated to stronger roll imprints, confirmed by the results of Fig. 2f.

The WindSat wind speed estimates have low variability, with values between 10.0 m s^{-1} and 11.0 m s^{-1} and an accuracy of 0.2 m s^{-1} (Zhang et al., 2018). Even if the wind speed is almost constant, the roll sizes are variable. Convective rolls are preferentially encountered when shear-induced turbulence dominates (Etling & Brown, 1993; Stopa et al., 2022). As the shear production is proportional to the cube of the surface velocity, the wind intensity is a key parameter in the development of these coherent structures but it is not the exclusive source of roll size variability. Based only on one case study, these results should be considered with caution. Such analysis should be applied on all the SAR wide swath images available during the EUREC4A field campaign to document the diversity of large-scale conditions.

4 Shallow Convection and Cold Pools

Figure 3b illustrates the results of identification method on an isolated feature in the south of the SAR swath. From the detected contours of the cold pool (orange lines), an ellipse can be fitted (green circle), and morphological characteristics of the detected feature can be derived, such as the size, the centroid, the flatness and the orientation. Also, dynamic properties can be inferred from the backscatter variability into the detected contours. Thus, the intensity of the gust front gradient at the forward edge (Fig. 3c), equal to 4.09×10^{-2} dB km^{-1} can be indicative of an active cold pool. The localized roughness maximum (yellow contour in Fig. 3a), equal to 4.16×10^{-1} dB is representative of a splash zone. In SAR observations, the origin of such strong localized σ_0 increase can be ambiguous between a rain signature (Alpers et al., 2016) or a disturbance of the signal due to the hydrometeors in the upper part of a deep convective system (Alpers et al., 2021). Only shallow convective clouds were encountered during EUREC4A, with cloud tops around 2 km - 3 km and no ice hydrometeors. Therefore, such roughness peaks are related to a splash zone, associated with rain cells.

The superposition of GOES T_B on SAR σ_0 at the same time (Fig. 3d) highlights the strong correlation between the cold pool imprint on the sea surface roughness and the cloud organization. Based on the synoptic conditions, the large patch of T_B colder than 280 K in the northwest of the cold pool, is due to high-level clouds with a north eastward advection typical of the atmospheric layer above the south westward trade wind flow. There is no apparent signature on the surface, these high clouds are completely decoupled of the MABL. However, a relative minimum in T_B that can be associated to an ascending core is observed above the cold pool. In addition to the collocated SAR – GOES superposition in time, a tracking of the cloud cold core ($T_B \leq 285$ K) is performed (Fig. 3e). At the SAR timing, the high altitude cloud layer interferes with the shallow convection clouds but the distinction is noticeable as soon as we go back 5 min before. The progressive growth of the cloud from its origin is observed. The 285 K level for this cloud was first detected at 0810 UTC at about 61 km upwind with a growth factor of 1.4 km^2 min^{-1} during the first hour following its detection. This backward tracking allows to explore the origin of the cloud entity and provides an estimate of the cold pool lifetime up to the present time, which in this case is about 1 hour.

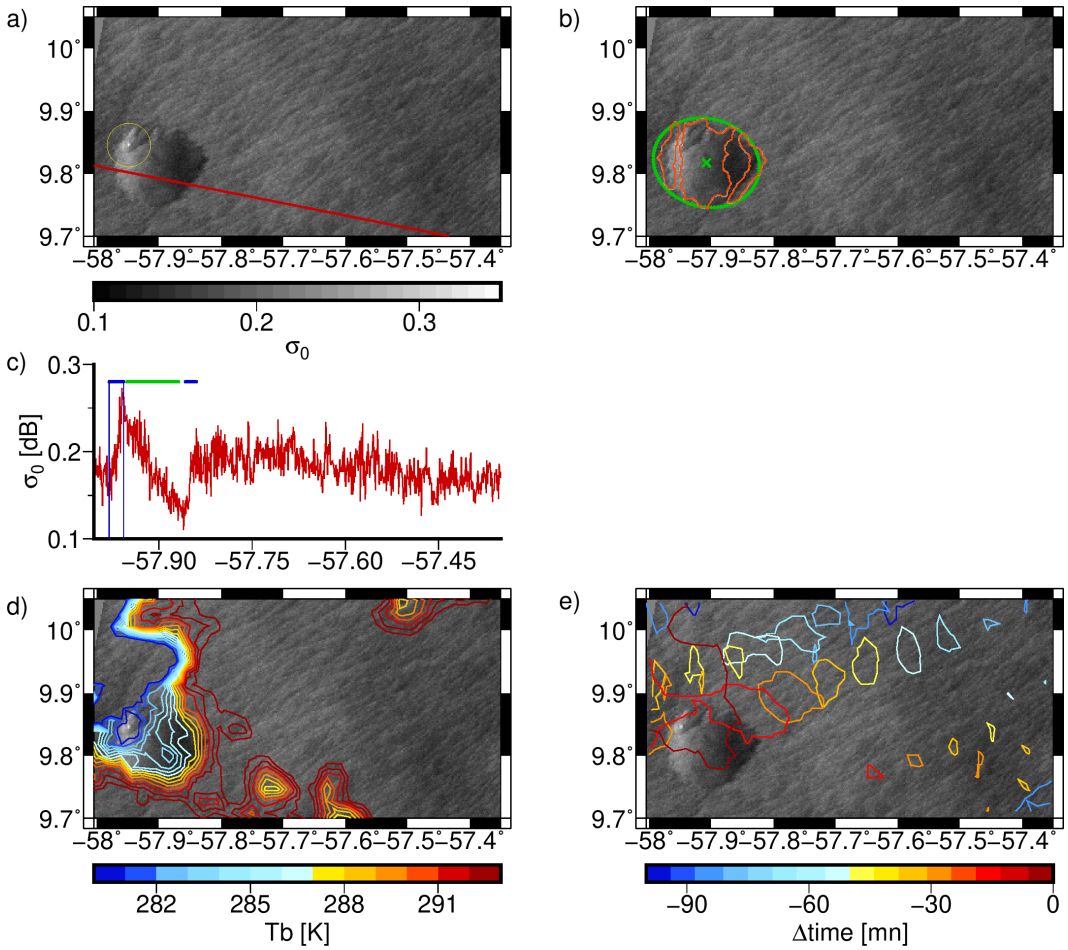

Figure 3. (a) SAR σ_0 centered on an isolated cold pool (red rectangle in Fig. 1). The yellow circle indicates a splash zone. (b) Results of the detection method (pink contours) and elliptical fit (green contours). (c) σ_0 transect along the red line shown in (a). (d) GOES T_B and SAR σ_0 contours superimposed at the same instant. (e) Backward tracking of the cloud cold core.

On the covered area, 68 cold pools have been identified (Fig. 4a). Most of them are located below the mesoscale shallow clouds in the center of the image. Due to interactions and collisions between them, these cold pools present a wide variability of sizes, shapes and orientations. Cold pools associated with isolated clouds have a smaller variability of geometric parameters and are generally smaller than the aggregated cold pools. The deduced morphological and dynamic cold pool metrics allow us to explore the physical processes involved. In particular, a correlation between the cold pool size and the maximum of σ_0 over the cold pool is found (Fig. 4b). As long as the cold pool is energetically supplied by the cloud above, the latter is still expanding. Furthermore, these convective systems induce a high σ_0 maximum either related to splash zones directly due to the rain or to an increase of the wind intensity associated with gust fronts. The more active cold pools have a stronger roughness contrast (maximum of σ_0) with their environment and thus a sharper edge gradient related to the gust front gradient intensity (Fig. 4e).

The combination of GOES T_B and SAR σ_0 allows us to explore the connections between the cloud layer and the cold pool dynamics. A backward tracking of the clouds with cold cores allows us to define the parameters $\Delta_{\text{life}}T_B$ as the difference between the minimum of T_B at the present time and that obtained since the cloud birth. If $\Delta_{\text{life}}T_B$ is equal to 0, the T_B minimum is reached at the present time, and the higher $\Delta_{\text{life}}T_B$, means that the actual cloud is certainly dissipating. A tendency emerges, with less intense cold pool gust front gradients for higher $\Delta_{\text{life}}T_B$ (Fig. 4c). This reflects a coupled loss of convective intensity both in the cloud layer and at the surface, with weakening convective motions within clouds and potentially dissipating cold pools. The spatial variability of the T_B over a cloud is estimated through the parameter $\Delta_{\text{shield}}T_B$. For a given cloud, $\Delta_{\text{shield}}T_B$ is the difference between the minimum of T_B over the cloud and the averaged T_B over the entire cloud. It provides insight into how active the cloud is, a more negative $\Delta_{\text{shield}}T_B$ indicates the existence of cold cores and localized vertical developments. Higher σ_0 maxima are associated to more negative $\Delta_{\text{shield}}T_B$ (Fig. 4d), which allows us to connect the more intense cold pool imprint seen from below at the surface, to the intensity of the convective activity seen from above.

5 Conclusions

An extensive analysis of a wide swath SAR image has been performed with the combined use of in situ airborne measurement and geostationary T_B. The SAR σ_0 provides a quasi-instantaneous picture of the sea surface roughness. The signatures of MABL coherent structures into convective rolls under suppressed conditions and of cold pools below clouds have been analyzed.

The intercomparison of the observed structures on the sea surface roughness with w' measured by the ATR 42 aircraft has allowed to consolidate the hypothesis of a significant relationship between the surface small scales and the MABL processes. The spatial variability of MABL organization has been captured with 2D autocorrelation analysis performed over 25×25 km^2 sub-domains of the SAR wide swath. Convective rolls were the predominant coherent structures. These rolls are almost oriented in the mean surface wind direction with characteristic scales between 2.0 and 3.9 km. The cell/roll transition zones have been mainly observed in the surrounding environment of the mesoscale cloud patterns.

Shallow convection has been investigated with an innovative approach, combining SAR σ_0 and GOES T_B in order to access the dynamics of clouds as seen from below and above. An identification method has been developed to detect the cold pools on σ_0. The characteristics of the cold pools, based on geometrical or physically-based metrics are thus extracted. A large number of cold pools have been identified over the covered area with significant variability in their properties. The more active cold pools, associated with

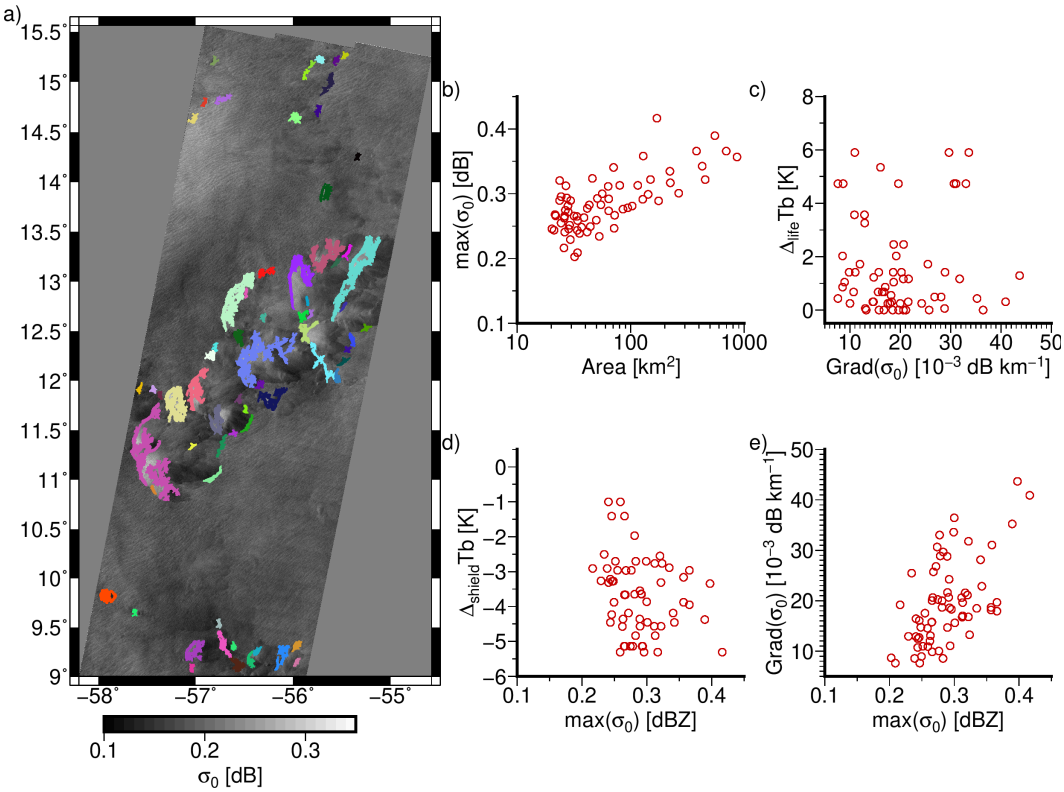

Figure 4. (a) Detected cold pools over the entire large swath, each color refers to a different object, (b) σ_0 maximum as a function of the cold pool size, (c) $\Delta_{\text{life}}T_B$ as a function of the gust front gradient intensity, (d) $\Delta_{\text{shield}}T_B$ versus the σ_0 maximum and (e) gust front gradient intensity as a function of σ_0 maximum.

a higher cloud dynamic intensity, present sharper edge σ_0 contrasts and higher σ_0 maxima. The intensity of the cloud activity, associated with cold cores and pronounced vertical developments up to 2 km, has been connected to the strong cold pool imprint on sea surface roughness. Also, the relation between the decrease of convective intensity in the cloud layer and the dissipating cold pools at the surface has been noted.

The new perspectives, presented here with a case study, can pave the way to improve our understanding of MABL processes from satellite observations. This study also highlights the importance of in situ data, and more intercomparisons can deeply strengthen the inferences. This requires a real overlap between platforms and an adapted aircraft sampling strategy. The opportunity to jointly analyze characteristics of cold pools and related convection cloud organization, which can take a spectacular variety of forms and shapes should provide significant insights into the mechanisms involved. The next step is to apply our approach to an ensemble of varying conditions, targeting other regions and both shallow and deep convection. The surrounding environment and its interplay with the cloud systems are also of great interest.

6 Open Research

Sentinel-1 is part of the European space component of the Copernicus European program. level-1 GRD data are free of charge and available on the Copernicus Open Access Hub (`https://sentinels.copernicus.eu/web/sentinel/sentinel-data-access`). GOES-16 ABI Level 1b radiances are available at `https://doi.org/10.7289/V5BV7DSR`. WindSat data are produced by Remote Sensing Systems and sponsored by the NASA Earth Science MEaSUREs DISCOVER Project and the NASA Earth Science Physical Oceanography Program. RSS WindSat data are available at `https://data.remss.com/windsat/`. The EUREC4A turbulence dataset derived from the SAFIRE ATR 42 aircraft is available on the AERIS database (`https://doi.org/10.25326/128`).

Acknowledgments

The EUREC4A project provided a relevant framework for this study. PEB and AA were supported through a Postdoctoral Grant funded by the Centre National d'Études Spatiales (CNES). Airborne data were obtained from the ATR aircraft operated by SAFIRE, the French facility for airborne research, an infrastructure of the CNRS, Météo-France and the CNES. AM was supported by the ESA Sentinel-1 Mission Performance Center (4000107360/12/I-LG). We also thanks the CNES which provide, through the TOSCA PROCONUM project (Pi. DB) the facilities for authors to collaborate.

References

Alpers, W., & Brümmer, B. (1994). Atmospheric boundary layer rolls observed by the synthetic aperture radar aboard the ers-1 satellite. *Journal of Geophysical Research: Oceans*, *99*(C6), 12613-12621. doi: https://doi.org/10.1029/94JC00421

Alpers, W., Zhang, B., Mouche, A., Zeng, K., & Chan, P. W. (2016). Rain footprints on c-band synthetic aperture radar images of the ocean - revisited. *Remote Sensing of Environment*, *187*, 169-185. doi: https://doi.org/10.1016/j.rse.2016.10.015

Alpers, W., Zhao, Y., Mouche, A. A., & Chan, P. W. (2021). A note on radar signatures of hydrometeors in the melting layer as inferred from sentinel-1 sar data acquired over the ocean. *Remote Sensing of Environment*, *253*, 112177. doi: https://doi.org/10.1016/j.rse.2020.112177

Atkinson, B. W., & Wu Zhang, J. (1996). Mesoscale shallow convection in the atmosphere. *Reviews of Geophysics*, *34*(4), 403-431. doi: https://doi.org/10.1029/

96RG02623

Atlas, D. (1994). Footprints of storms on the sea: A view from spaceborne synthetic aperture radar. *Journal of Geophysical Research: Oceans*, *99*(C4), 7961-7969. doi: https://doi.org/10.1029/94JC00250

Atlas, D., Iguchi, T., & Pierce, H. F. (1995). Storm-induced wind patterns on the sea from spaceborne synthetic aperture radar. *Bulletin of the American Meteorological Society*, *76*(9), 1585 - 1592. doi: 10.1175/1520-0477(1995)076⟨1585:SIWPOT⟩2.0.CO;2

Ayet, A., Rascle, N., Chapron, B., Couvreux, F., & Terray, L. (2021). Uncovering air-sea interaction in oceanic submesoscale frontal regions using high-resolution satellite observations. *US Clivar variations*, *19*(1). doi: https://doi.org/10.5065/ybca-0s03

Bony, S., Lothon, M., Delanoë, J., Coutris, P., Etienne, J.-C., Aemisegger, F., ... Vogel, R. (2022). EUREC^{4}A observations from the SAFIRE ATR42 aircraft. *Earth System Science Data Discussions*, *2022*, 1–61. doi: 10.5194/essd-2021-459

Brient, F., Couvreux, F., Villefranque, N., Rio, C., & Honnert, R. (2019, March). Object-Oriented Identification of Coherent Structures in Large Eddy Simulations: Importance of Downdrafts in Stratocumulus. *Geophysical Research Letters*, *46*(5), 2854–2864. doi: https://doi.org/10.1029/2018GL081499

Brilouet, P.-E., Lothon, M., Etienne, J.-C., Richard, P., Bony, S., Lernoult, J., ... Charoy, T. (2021). The EUREC^{4}A turbulence dataset derived from the SAFIRE ATR 42 aircraft. *Earth System Science Data Discussions*, *2021*, 1–28. doi: 10.5194/essd-2021-52

Brown, R. A. (1980). Longitudinal instabilities and secondary flows in the planetary boundary layer: A review. *Reviews of Geophysics*, *18*(3), 683-697. doi: https://doi.org/10.1029/RG018i003p00683

de Szoeke, S. P., Skyllingstad, E. D., Zuidema, P., & Chandra, A. S. (2017). Cold pools and their influence on the tropical marine boundary layer. *Journal of the Atmospheric Sciences*, *74*(4), 1149 - 1168. doi: https://doi.org/10.1175/JAS-D-16-0264.1

Etling, D., & Brown, R. A. (1993). Roll vortices in the planetary boundary layer: A review. *Boundary-Layer Meteorology*, *65*(3), 215–248. doi: https://doi.org/10.1007/BF00705527

Garg, P., Nesbitt, S. W., Lang, T. J., Priftis, G., Chronis, T., Thayer, J. D., & Hence, D. A. (2020). Identifying and characterizing tropical oceanic mesoscale cold pools using spaceborne scatterometer winds. *Journal of Geophysical Research: Atmospheres*, *125*(5), e2019JD031812. doi: https://doi.org/10.1029/2019JD031812

Granero-Belinchon, C., Roux, S., Garnier, N., Tandeo, P., Chapron, B., & Mouche, A. (2022). Two-dimensional structure functions to characterize convective rolls in the marine atmospheric boundary layer from sentinel-1 SAR images. doi: https://hal.archives-ouvertes.fr/hal-03576400

Grossman, R. L. (1982). An analysis of vertical velocity spectra obtained in the bomex fair-weather, trade-wind boundary layer. *Boundary-Layer Meteorology*, *23*(3), 323–357. doi: https://doi.org/10.1007/BF00121120

Kilpatrick, T. J., & Xie, S.-P. (2015). Ascat observations of downdrafts from mesoscale convective systems. *Geophysical Research Letters*, *42*(6), 1951-1958. Retrieved from `https://agupubs.onlinelibrary.wiley.com/doi/abs/10.1002/2015GL063025` doi: https://doi.org/10.1002/2015GL063025

Kudryavtsev, V., Akimov, D., Johannessen, J., & Chapron, B. (2005). On radar imaging of current features: 1. model and comparison with observations. *Journal of Geophysical Research: Oceans*, *110*(C7). doi: https://doi.org/10.1029/2004JC002505

La, T. V., Messager, C., Honnorat, M., Sahl, R., Khenchaf, A., Channelliere, C., & Lattes, P. (2020). Use of sentinel-1 c-band sar images for convective system surface wind pattern detection. *Journal of Applied Meteorology and Climatology*, *59*(8), 1321 - 1332. doi: https://doi.org/10.1175/JAMC-D-20-0008.1

LeMone, M. A. (1973). The structure and dynamics of horizontal roll vortices in the planetary boundary layer. *Journal of Atmospheric Sciences*, *30*(6), 1077 - 1091. doi: https://doi.org/10.1175/1520-0469(1973)030⟨1077:TSADOH⟩2.0.CO;2

LeMone, M. A., & Pennell, W. T. (1976). The relationship of trade wind cumulus distribution to subcloud layer fluxes and structure. *Monthly Weather Review*, *104*(5), 524 - 539. doi: 10.1175/1520-0493(1976)104⟨0524:TROTWC⟩2.0.CO;2

Lohou, F., Druilhet, A., Campistron, B., Redelspergers, J.-L., & Saïd, F. (2000). Numerical study of the impact of coherent structures on vertical transfers in the atmospheric boundary layer. *Boundary-layer meteorology*, *97*(3), 361–383. doi: 10.1023/A:1002641728075

Mapes, B., Milliff, R., & Morzel, J. (2009). Composite life cycle of maritime tropical mesoscale convective systems in scatterometer and microwave satellite observations. *Journal of the Atmospheric Sciences*, *66*(1), 199 - 208. doi: https://doi.org/10.1175/2008JAS2746.1

Schmit, T. J., Gunshor, M. M., Menzel, W. P., Gurka, J. J., Li, J., & Bachmeier, A. S. (2005). Introducing the next-generation advanced baseline imager on goes-r. *Bulletin of the American Meteorological Society*, *86*(8), 1079 - 1096. doi: https://doi.org/10.1175/BAMS-86-8-1079

Stevens, B., Bony, S., Brogniez, H., Hentgen, L., Hohenegger, C., Kiemle, C., ... Zuidema, P. (2020). Sugar, gravel, fish and flowers: Mesoscale cloud patterns in the trade winds. *Quarterly Journal of the Royal Meteorological Society*, *146*(726), 141-152. doi: https://doi.org/10.1002/qj.3662

Stopa, J. E., Wang, C., Vandemark, D., Foster, R., Mouche, A., & Chapron, B. (2022). Automated global classification of surface layer stratification using high-resolution sea surface roughness measurements by satellite synthetic aperture radar. *Geophysical Research Letters*, *49*(12), e2022GL098686. doi: https://doi.org/10.1029/2022GL098686

Vandemark, D., Mourad, P. D., Bailey, S. A., Crawford, T. L., Vogel, C. A., Sun, J., & Chapron, B. (2001). Measured changes in ocean surface roughness due to atmospheric boundary layer rolls. *Journal of Geophysical Research: Oceans*, *106*(C3), 4639-4654. doi: https://doi.org/10.1029/1999JC000051

Villefranque, N., Williamson, D., Couvreux, F., Hourdin, F., Gautrais, J., Fournier, R., ... Volodina, V. (2020). Process-based climate model development harnessing machine learning: Iii. the representation of cumulus geometry and their 3d radiative effects. *Earth and Space Science Open Archive*, 30. doi: https://doi.org/10.1002/essoar.10505088.1

Vogel, R., Konow, H., Schulz, H., & Zuidema, P. (2021). A climatology of trade-wind cumulus cold pools and their link to mesoscale cloud organization. *Atmospheric Chemistry and Physics*, *21*(21), 16609–16630. doi: https://doi.org/10.5194/acp-21-16609-2021

Wang, C., Mouche, A., Foster, R. C., Vandemark, D. C., Stopa, J. E., Tandeo, P., ... Chapron, B. (2019). Characteristics of Marine Atmospheric Boundary Layer Roll Vortices from Sentinel-1 Sar Wave Mode. *IGARSS 2019 - 2019 IEEE International Geoscience and Remote Sensing Symposium*, 7908-7911. doi: https://doi.org/10.1109/IGARSS.2019.8900287

Wang, C., Vandemark, D., Mouche, A., Chapron, B., Li, H., & Foster, R. C. (2020). An assessment of marine atmospheric boundary layer roll detection using sentinel-1 sar data. *Remote Sensing of Environment*, *250*, 112031. doi: https://doi.org/10.1016/j.rse.2020.112031

Wentz, F., Ricciardulli, L., C.Gentemann, Meissner, T., Hilburn, K., & Scott, J. (2013). Remote sensing systems coriolis windsat daily environmental suite on 0.25 deg grid, version 7.0.1. (Available online at `www.remss.com/missions/windsat`)

Young, G. S., Kristovich, D., Hjelmfelt, M., & Foster, R. (2002, 07). Rolls, streets, waves, and more: A review of quasi-two-dimensional structures in the atmospheric boundary layer. *Bulletin of The American Meteorological Society - BULL AMER METEOROL SOC*, *83*. doi: 10.1175/1520-0477(2002)083⟨0997:RSWAMA⟩2.3.CO;2

Young, G. S., Sikora, T. D., & Winstead, N. S. (2000). Inferring marine atmospheric boundary layer properties from spectral characteristics of satellite-borne sar imagery. *Monthly Weather Review*, *128*(5), 1506 - 1520. doi: 10.1175/1520-0493(2000)128⟨1506:IMABLP⟩2.0.CO;2

Zhang, L., Shi, H., Wang, Z., Yu, H., Yin, X., & Liao, Q. (2018). Comparison of wind speeds from spaceborne microwave radiometers with in situ observations and ecmwf data over the global ocean. *Remote Sensing*, *10*(3). doi: https://doi.org/10.3390/rs10030425

Zuidema, P., Li, Z., Hill, R. J., Bariteau, L., Rilling, B., Fairall, C., ... Hare, J. (2012). On trade wind cumulus cold pools. *Journal of the Atmospheric Sciences*, *69*(1), 258 - 280. doi: https://doi.org/10.1175/JAS-D-11-0143.1